Robust Adaptive Segmentation of 3D Medical Images with Level Sets

Caroline Baillard, Christian Barillot, Patrick Bouthemy

INSTITUT NATIONAL DE RECHERCHE EN INFORMATIQUE ET EN AUTOMATIQUE

Robust Adaptive Segmentation of 3D Medical Images with Level Sets

C. Baillard , C. Barillot , P. Bouthemy

N˚4071

Novembre 2000

THÈME 3

ISSN 0249-6399 ISRN INRIA/RR--4071--FR+ENG

Robust Adaptive Segmentation of 3D Medical Images with Level Sets

C. Baillard , C. Barillot , P. Bouthemy

Thème 3 — Interaction homme-machine,
images, données, connaissances
Projet Vista

Rapport de recherche n˚4071 — Novembre 2000 — 26 pages

Abstract: This paper is concerned with the use of the Level Set formalism to segment anatomical structures in 3D medical images (ultrasound or magnetic resonance images). A closed 3D surface propagates towards the desired boundaries through the iterative evolution of a 4D implicit function. The major contribution of this work is the design of a robust evolution model based on adaptive parameters depending on the data. First the step size and the external propagation force factor, both usually predetermined constants, are automatically computed at each iteration. Additionally, region-based information, rather than spatial image gradient, is exploited by estimating intensity probability density functions over the image. As a result, the method can be applied to various kinds of data. Quantitative and qualitative results on brain MR images and 3D echographies of carotid arteries are reported and discussed.

Key-words: 3D segmentation, deformable models, level sets, intensity distribution, brain MRI, 3D ultrasound images

(Résumé : tsvp)

Unité de recherche INRIA Rennes
IRISA, Campus universitaire de Beaulieu, 35042 RENNES Cedex (France)
Téléphone : 02 99 84 71 00 - International : +33 2 99 84 71 00
Télécopie : 02 99 84 71 71 - International : +33 2 99 84 71 71

Segmentation adaptative et robuste d'images 3D médicales par des ensembles de niveaux

Résumé : Ce papier s'intéresse au formalisme des ensembles de niveaux pour segmenter des structures anatomiques dans des images médicales 3D (ultrasons ou images de résonance magnétiques). Une surface 3D fermée se propage vers les contours désirés par l'évolution itérative d'une fonction 4D implicite. La contribution majeure de ce travail est la définition d'un modèle d'évolution robuste basé sur l'utilisation de paramètres adaptatifs aux données. Le pas d'itération et le poids de la force de propagation externe sont calculés automatiquement à chaque itération, ces deux paramètres étant habituellement prédéterminées comme constants. En outre, une information basée région, plutôt que le gradient spatial de l'image, est exploitée en estimant des densités de probabilité de la fonction d'intensité-image. En conséquence, la méthode peut être appliquée à plusieurs types de données. Des résultats quantitatifs et qualitatifs sur des images IRM du cerveau et des échographies 3D d'artères carotides sont montrés et discutés.

Mots-clé : segmentation 3D, modèles déformables, ensembles de niveaux, distribution d'intensités, IRM cérébale, ultrasons 3D

1 Introduction

The 3D segmentation of anatomical structures is crucial for many medical applications, both for visualization and clinical diagnosis purposes. Due to the huge amount of data and the complexity of these structures, manual segmentation is extremely tedious and often inconsistent. Automatic segmentation methods are required to fully exploit 3D data. It is a very challenging task because they can not usually rely on image information only. Anatomical tissues are not homogeneous and their boundaries are not clearly defined in the images. It is often necessary to use prior knowledge about the shape or the image properties of the structure of interest.

Deformable models define a powerful tool to accurately recover a structure using very few assumptions about its shape. They are parametrized curves or surfaces which iteratively evolve towards the desired location according to an energy minimization process [30]. The energy function is based on external forces derived from the data (high image gradient for instance), and internal forces related to the geometry of the contour itself (typically the curvature). Active contours have been widely used and they are very successful to extract edges and lines for instance [14]. A significant advantage of deformable models is their ability to take into account global *prior* knowledge about the expected shape and its variability. The model evolution towards the desired location can for instance be constrained by statistical information about the object shape [15, 17, 22]. The limitations of deformable models are well-known. The contour evolution is very sensitive to initial position because of the multiple minima of the energy function. Besides, due to the explicit parametrization of the model and the need for internal forces, deformable contours cannot cope with significant protusions and topological changes. Therefore the initialization must be reasonably close to the desired location, and the topology is required to be known before the process starts. Some extensions have been proposed in order to prevent the contour from getting trapped by isolated spurious edges, for instance by using an inflating force [7] or region-based information [6, 37]. Stronger constraints about the shape can also be used (parametrized templates for instance), but some details are then lost, and designed solutions are then rather dedicated to the problem at hand [29].

An alternative solution to energy minimization approaches consists in considering the contour evolution as a front propagation problem [4, 19]. The major interest of this approach lies in the possibility of using the *Level Set* formalism, which was first introduced by Osher and Sethian to model propagating fronts with curvature-dependent speeds [23]. It provides powerful numerical techniques for analysing and computing interface motion and more generally for solving evolution problems based on partial differential equations. The iterative techniques based on the Level Set formalism have proved particularly appropriate for segmenting complex 3D anatomical shapes [12, 35]. The detected surface can change its topology and cope with significant protusions, and the result is less dependent on initialization than with any other iterative method.

Within the Level Set formulation, the 3D object to be segmented is represented by an evolving closed 3D surface. This surface is embedded as the zero level of a 4-dimensional scalar function Ψ. The surface evolution can then be described through the evolution of the implicit function Ψ in a fixed coordinate system (Eulerian description). This implicit representation allows the front to change topology. This approach has already been applied within a wide range of applications in computer vision: morphological filtering, tracking, shape from shading, stereovision, etc. Initially proposed

for 2D data, the extension to 3D is straighforward. However, model parametrization is a limitation for practical use. Several evolution models have been proposed, but most of them include many parameters or factors to be tuned: step size, weighting parameters, additive propagation term, etc. The appropriate setting of these parameters strongly influences the performance of the methods. In a medical context, the user does not usually have the background to tune a large number of parameters, especially if this tuning does not result on effects he can immediately evaluate. Therefore an adaptive solution is required for clinical applications.

This paper describes a robust and adaptive evolution model which enables a volume to be segmented with minimal manual parameter setting. The model is related to region-based information rather than image gradient. More precisely it is based on the estimation of intensity probability density functions over the image. The versatility of our segmentation method is demonstrated by reporting results on both brain structures in MR images and carotid arteries in 3D echography. The remainder of this paper is organized as follows. Our strategy is presented in Section 2. The two main stages of the method - intensity distribution analysis and surface evolution - are respectively described in Sections 3 and 4. A numerical assessment and several results are reported and discussed in Section 5. Section 6 contains concluding remarks.

2 Segmentation Based on Level Sets

The segmentation problem is expressed as the computation of a 3D surface $S(t)$ (or front) propagating in time along its normal direction. In the level set formulation [23], the propagating front $S(t)$ is embedded as the zero level of a time-varying higher dimensional function $\Psi(\mathbf{X}, t)$:

$$S(t) = \{\mathbf{X} \in I\!R^3 \,/\, \Psi(\mathbf{X}, t) = 0\} \tag{1}$$

The function Ψ describes a 4-D surface defined by $\Psi(\mathbf{X}, t) = d$, where d is traditionnally the signed distance from $\mathbf{X}$ to the front S (negative *inside* the object). The evolution rule for Ψ can be expressed as:

$$\frac{\partial \Psi}{\partial t} + F|\nabla \Psi| = 0, \tag{2}$$

where F is a scalar speed function depending on:

- local properties of the front, like the local curvature,
- external parameters related to the input data (image gradient for instance),
- additional propagation terms.

The 4D surface Ψ deforms iteratively according to F, and the position of the 3D front $S(t)$ is deduced from Ψ at each iteration by the relation $\Psi(\mathbf{X}, t) = 0$. Practically, the hypersurface Ψ^{n+1} at step $n + 1$ is computed from Ψ^n at step n using the relation:

$$\Psi^{n+1}(\mathbf{X}) = \Psi^n(\mathbf{X}) - \Delta t.F|\nabla \Psi^n(\mathbf{X})|, \quad \forall \mathbf{X} \in I\!R^3 \tag{3}$$

The design of the speed function F plays the major role in the evolution process. Several formulations have been proposed [4, 11, 25, 36]. The original formulation was given by Malladi [19]:

$$F = h_I(\nu - \rho\kappa), \tag{4}$$

where:

- ν represents an external propagation force which makes the surface contract or expand;
- κ is the local curvature of the front and acts as a regularization term;
- ρ is a weighting parameter expressing the importance given to regularization;
- h_I is the data consistency term and acts as a stopping criterion at the location of the desired boundaries; it depends on the intensity function *I*.

In this work, a robust evolution model involving adaptive parameters has been designed. It is defined with respect to the input data and to statistical distribution models. In the following, our definition of the parameters introduced in equations (3) and (4) is presented. They are related to intensity probability density functions (PDFs) estimated *inside* and *outside* the structure to be segmented. These two PDFs will be respectively denoted $p_i(u)$ and $p_e(u)$, where $u = I(x, y, z)$ is the intensity value at the voxel of coordinates (x, y, z). The prior probability for a voxel to be *inside* the structure will be denoted α_i. Our general strategy is outlined in Figure 1. Probability functions p_i, p_e and α_i are first estimated using the initial segmentation and given statistical distribution models. This allows the parameters of the speed function to be computed for the evolution of the hypersurface. The parameter estimation and the evolution model are respectively described in the next two sections.

3 Estimation of intensity Probability Density Functions

We assume that the intensity function of the input image can be modeled as a mixture of n distributions. Furthermore, these distributions do not necessarily have the same form. For example, the Rayleigh distribution is more appropriate than the Gaussian distribution to model signal in 3D echography [22]. In this work, we have considered two kinds of laws: the Gaussian distribution and the shifted Rayleigh distribution. The latter is given by:

$$\mathcal{R}(u; c, \alpha) = \frac{u - c}{\alpha^2} exp(-\frac{(u - c)^2}{2\alpha^2}), \tag{5}$$

where c and α are the two parameters characterizing the Rayleigh distribution.

Each distribution is associated to a class labelled by λ_k and described by the vector Φ_k consisting of three parameters: the two parameters characterizing the distribution model (mean and standard deviation for a Gaussian; c and α for a Rayleigh distribution) and the prior probability $P(\lambda_k) = \pi_k$ of a voxel belonging to class λ_k.

The distribution mixture is thus described by vector $\Phi = \{\Phi_k, 1 \leq k \leq n\}$. We start by estimating Φ using the Stochastic Expectation-Maximisation (SEM) algorithm [5, 21]. The SEM algorithm aims at determining the various components of a mixture of probability distributions. It is a stochastic version of the EM algorithm [9] which utilizes a probabilistic learning stage. First, only an overestimate of the number of components is required. Second, it is less dependent on initialization than the EM algorithm.

Let n be an upper bound of the number of components, and δ be a threshold in $]0, 1]$. The algorithm is initialized with the initial vectors $\Phi^{[0]} = \{\Phi_k^{[0]}, 1 \leq k \leq n\}$, and the initial prior probabilities proportions $\pi_k^{[0]}$. Given vectors $\Phi^{[p]} = \{\Phi_k^{[p]}, 1 \leq k \leq n\}$ and $\pi_k^{[p]}$ at step p, the vector $\Phi^{[p+1]}$ at step $p+1$ is computed within three stages :

1. *Expectation:* The posterior probabilities $P(k|I, \Phi_k^{[p]})$ are estimated for each k with respect to $\Phi^{[p]}$ using Bayes rule:

$$P(k|I, \Phi^{[p]}) = \frac{\pi_k^{[p]} P(I|k, \Phi^{[p]})}{\sum_{q=0}^{q<n} \pi_q^{[p]} P(I|q, \Phi^{[p]})},$$

   where $\pi_k^{[p]}$ is the prior probability of component k estimated at step p.

2. *Stochastic:* Each voxel of the volume is associated with a class k by stochastic sampling according to the expected probabilities $P(k|I, \Phi_k^{[p]})$. This defines a partition of the volume.

3. *Maximization:* The vectors $\Phi_k^{[p+1]}$ and $\pi_k^{[p+1]}$ characterizing class k are estimated by maximizing the likelihood of class k over the complete data given by the partitionned volume. In particular, $\pi_k^{[p+1]}$ is estimated by the proportion $\widehat{\pi_k^{[p+1]}}$ of voxels belonging to class k in the volume. Furthermore, if there is a component k such as $\widehat{\pi_k^{[p+1]}} < \delta$, then the component k is removed from the set and the number of components n decreases of 1.

Thanks to the stochastic step, the SEM algorithm is less sensitive to initialization than the EM algorithm. However convergence is not guaranteed. Therefore the stopping criterion must be heuristically set and the algorithm might not find the global maximum of the likelihood surface. The initialization of Φ_k is therefore still important. For this initialization, we have distinguished two cases according to the value of n.

If $n = 2$, the distribution mixture is bimodal, i.e., the object to be segmented and the "background" can each be approximated by a single distribution. In this case, the surface initializing the segmentation process is exploited to produce two separate histograms from the input image: one for the object resulting from the initial segmentation and one for the background. The variables Φ_0 and Φ_1 characterizing the bimodal mixture are independently estimated over these complete data, providing two coarse estimates $\widehat{\Phi_0^{init}}$ and $\widehat{\Phi_1^{init}}$. We implicitely assume that the intensity distribution inside and outside the initial segmentation are somehow representative of the distributions to

be estimated. The bimodal approach is outlined in Figure 2. Figure 3 shows an example of PDFs estimated with this method for the image shown in Figure 11. Even though the bimodal model does not perfectly fit the distribution, it is nevertheless accurate enough to separate the two main classes of the image.

If the distribution is not bimodal, the parameter n is initialized to a value overestimating the number of classes. For instance, in the case of brain MR images (see Figure 8), n is initialized to 7, which is a typical starting value for this type of problem (e.g. [28]). The local maxima of the histogram are used as an initial guess for the center of the distribution kernels. The prior probabilities π_k are initialized as uniform. The parameters of the distributions other than the center (standard deviation in case of a Gaussian distribution or parameter α for a Rayleigh distribution) are initialized with an arbitrary value. This initial guess of vector Φ serves as initialization to the SEM algorithm, which provides an estimation of π_k and $P(I|\lambda_k)$ for each class λ_k.

Among these n classes, usually only one or two of them usually characterize the structure to be segmented. They will form the set denoted Λ_i. The complementary set consisted of classes corresponding to the background will be denoted Λ_e. We now need to separate the classes belonging to Λ_i from those belonging to Λ_e. The number of classes defining Λ_i and a typical intensity value characterizing each of them can be given by the user. Alternatively they can be automatically determined from the initialization of the surface (required for the segmentation process): only the classes "highly" represented *inside the initial surface* are stated as belonging to Λ_i.

More precisely, the intensity distribution over the whole image can be explicitely written as:

$$\begin{aligned} P(u) &= \sum_{k=1}^{n} \pi_k P(u|\lambda_k) \\ &= \sum_{k=1}^{n} (\pi_k^i + \pi_k^e) P(u|\lambda_k), \end{aligned} \tag{6}$$

where π_k^i (resp. π_k^e) is the proportion ratio of class λ_k inside (resp. outside) the initial surface segmenting the object of interest.

In order to determine an estimate of π_k^i for each class k, we fit a mixture distribution to the intensity histogram computed inside the initial surface, using the distribution parameters obtained previously on the whole image. Classification is then achieved as follows:

$$\lambda_k \in \Lambda_i \Leftrightarrow \frac{\pi_k^i}{\sum_{1 \leq k' \leq n} \pi_{k'}^i} > \pi_k \tag{7}$$

In other words, a component k of the mixture corresponds to the structure to be segmented if the proportion of voxels labelled as k inside the initial surface is superior to its proportion computed over the whole volume. This automatic determination of the components is a rather convenient and efficient way to identify the classes to deal with in the segmentation process, especially when several classes are concerned (segmentation of the union of grey matter and white matter in brain MRI for instance).

Once the sets Λ_i and Λ_e have been determined, the estimated intensity distributions inside and outside the object can be defined as:

$$\begin{cases} p_i(u) & = & \sum_{k/\lambda_k \in \Lambda_i} \pi_k P(u|\lambda_k) \\ p_e(u) & = & \sum_{k/\lambda_k \in \Lambda_e} \pi_k P(u|\lambda_k), \end{cases} \tag{8}$$

and the prior probability for a voxel to be inside the structure of interest is given by:

$$\alpha_i = \sum_{k/\lambda_k \in \Lambda_i} \pi_k \tag{9}$$

An example of multimodal distribution mixture estimated with this method is shown in Figure 4. The number of components was initialized to 7. The 5 main components of the brain structure have been recovered, and the 2 additional components were automatically removed during the process.

The SEM algorithm does not guarantee the optimal solution, but in practice, any initial partition roughly representative of the inner and the outer distributions leads to a correct solution. In particular, the initial surface does not need to be close to the real boundaries. However, if the initialization is not representative of the inner distribution (case of a very small sphere inside the object for instance), a coarse segmentation could be first produced with a classical version of the speed function, where the stopping factor h_I is based on image gradients and the external propagation force factor ν is constant for instance (see Section 4).

4 Evolution Model

4.1 External propagation factor ν

In equation (4), the sign of factor ν determines the direction of the external propagation force. Several approaches to 3D segmentation using this evolution model have imposed a one-way propagation force ν, which either contracts or expands the whole surface all along the process [18, 36]. However, when the initial position of the surface can be predicted (by tracking, or by registration with an atlas for instance), the predicted and real positions usually overlap. It is therefore necessary to let the surface evolve in both directions. Some propagation models have been designed in order to solve this problem in 2D, by performing a local analysis of intensity [1, 24, 33].

The problem can be expressed as the classification of each point of the current interface $S(t)$. If a point belongs to the object then the surface should locally extend; if it does not, the surface should contract. We perform this classification by maximizing the posterior segmentation probability $P(\lambda|u)$, where λ denotes the appartenance class of the considered point. According to Bayes rule, the maximization of the posterior distribution $P(\lambda|u)$ is equivalent to the maximization of $P(\lambda)P(u|\lambda)$, where $P(\lambda)$ is the *prior* of class λ and $P(u|\lambda)$ is the conditional likelihood of inten-

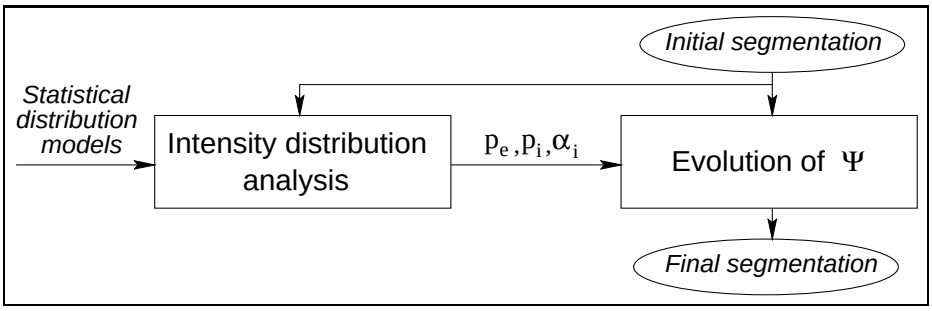

Figure 1: Strategy for 3D segmentation. The speed function, controlling the evolution of surface Ψ, is computed according to the estimated intensity density functions inside and outside the structure.

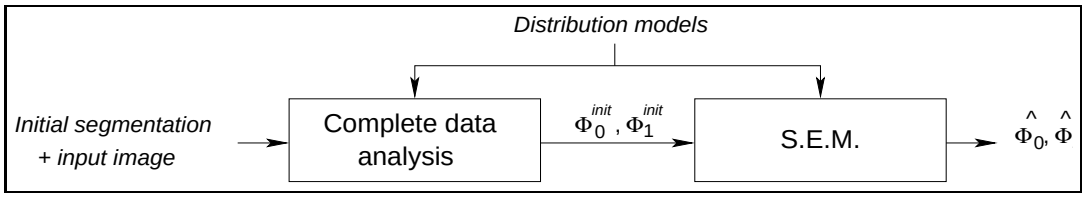

Figure 2: Strategy for estimating the mixture parameters when the distribution is bimodal.

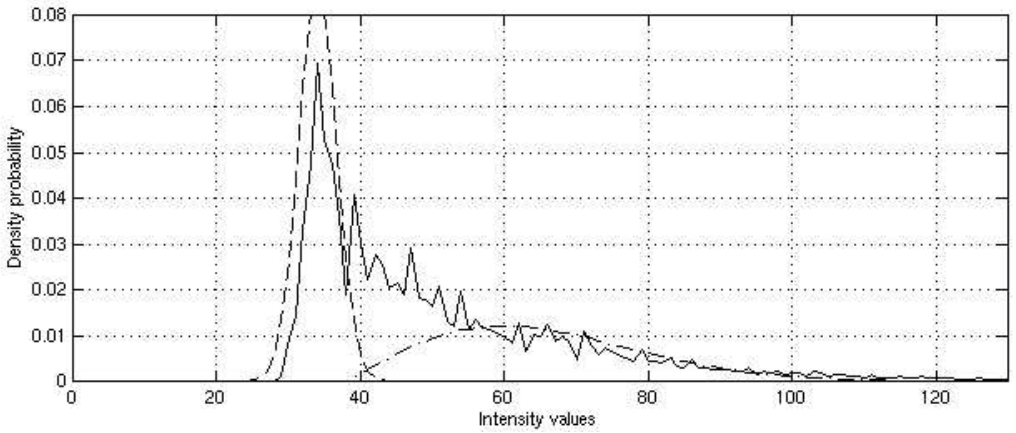

Figure 3: Estimation of the intensity mixture model parameters on the ultrasound image of Figure 11 (bimodal case). The solid line represents the normalized histogram of the input image. The dash line is the estimated PDF *inside* the carotid artery and the dashdot line is the estimated PDF *outside* it. Note, the estimated distribution mixture does not exactly fit the initial histogram because the bimodal approximation is too simple to accurately model the signal, nevertheless it is sufficient to produce an adequate segmentation.

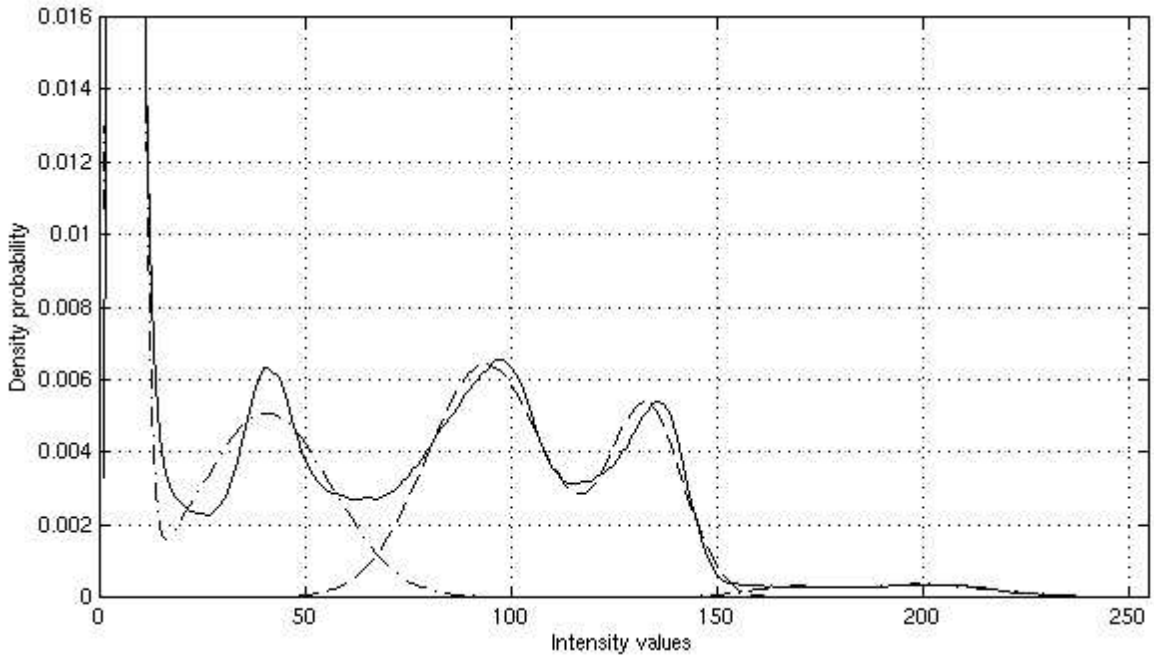

Figure 4: Estimation of the intensity mixture model parameters on brain MRI (multimodal case). The solid line represents the normalized histogram of the input image. The dash line is the estimated PDF *inside* the brain and the dashdot line is the estimated PDF *outside* the brain. The 5 main components of the brain structure have been recovered (i.e. background, spinal fluid, grey matter, white matter and skin/fat mixture).

sity. The propagation factor ν can then be defined as:

$$\begin{aligned} \nu &= \text{Sign}\{P(\lambda \in \Lambda_i|u) - P(\lambda \in \Lambda_e|u)\} \\ &= \text{Sign}\{\alpha_i p_i(u) - (1-\alpha_i)p_e(u)\}, \end{aligned} \tag{10}$$

where

$$\text{Sign}(x) = \begin{cases} +1 & \text{if } x \geq 0 \\ -1 & \text{if } x < 0 \end{cases}$$

The propagation factor ν is therefore positive at voxel u if $P(\lambda \in \Lambda_i|u) > P(\lambda \in \Lambda_e|u)$. This means that the surface extends where the interface point is more likely to be *inside* the object than *outside*. Note, we always have $\nu = \pm 1$. Experiments with a continous-varying function ν have not shown any improvement. Besides, this simple definition requires no tuning at all, which is very important in practice.

4.2 Curvature term

The regularization parameter κ at point $\mathbf{x}$ is defined in the usual way. It is the curvature of the interface, computed at the point of the interface which is the closest to $\mathbf{x}$, using the partial derivatives of Ψ :

$$\kappa_0 = \frac{(\Psi_{xx}+\Psi_{yy})\Psi_z^2 - 2\Psi_x\Psi_y\Psi_{xy} + (\Psi_{yy}+\Psi_{zz})\Psi_x^2 - 2\Psi_y\Psi_z\Psi_{yz} + (\Psi_{zz}+\Psi_{xx})\Psi_y^2 - 2\Psi_z\Psi_x\Psi_{zx}}{2(\Psi_x^2+\Psi_y^2+\Psi_z^2)^{1.5}}$$

The respective influences of the propagation and the regularization terms are entirely determined by the weight ρ, which makes the process very easy to tune. The weighting parameter ρ can be interpreted as the particular curvature radius leading to a stable position ($F = 0$). We have introduced two possible values for ρ according to the sign of the curvature κ:

$$\rho = \begin{cases} \rho^+ & \text{if } \kappa \geq 0 \\ \rho^- & \text{if } \kappa < 0 \end{cases} \tag{11}$$

For instance, the cortical sulci are characterized by a very high negative curvature. In order to improve the detection of these sulci in brain MRI, we use the values $\rho^- = 1$ and $\rho^+ = 3$.

4.3 Stopping factor h_I

The stopping factor h_I is a data consistency term usually related to the intensity gradient ∇I of the input image [19]. Since the image gradient is only defined for points belonging to the interface (zero level set of the hypersurface), an *extended* gradient function needs to be defined over $\mathbb{R}^3$: the intensity gradient at a given point of hypersurface Ψ will be given by the one at the closest neighbour on the interface. However, gradient information has no meaning for very noisy and/or low-contrasted images like ultrasound data. Besides, high image gradients do not necessarily indicate a relevant boundary between the structure to be segmented and its background (e.g. between grey and white matter on brain MRI).

Our approach is similar to the one described in [25] for the 2D case. We have related the stopping factor h_I to the *posterior* probability of having a transition between the object and its background. Let $\mathbf{x}$ be a voxel of the current interface, and λ the estimated class of $\mathbf{x}$. The posterior probability of $\mathbf{x}$ being a transition, given I and λ, is given by:

$$p_T(\mathbf{x}|I,\lambda) = \begin{cases} P(\mathbf{x}-\mathbf{n} \in \bar{\mathcal{O}}|I) & \text{if } \lambda \in \Lambda_i \\ P(\mathbf{x}-\mathbf{n} \in \mathcal{O}|I) & \text{if } \lambda \in \Lambda_e, \end{cases} \tag{12}$$

where $\mathbf{n} = \frac{\nabla\Psi}{|\nabla\Psi|}$ is the normal vector at point $\mathbf{x}$ of the hypersurface, $\mathcal{O}$ is the object to be segmented and $\bar{\mathcal{O}}$ its complementary. The voxel $\mathbf{x}' = \mathbf{x} - \mathbf{n}$ is a neighbouring voxel of $\mathbf{x}$ located outside the volume defined by hypersurface Ψ. Thus if $\mathbf{x}$ is more likely to be *inside* the object to be segmented ($\lambda \in \Lambda_i$), then the posterior transition probability of $\mathbf{x}$ is the probability of $\mathbf{x}'$ to be located *outside* the object to be segmented.

Under the assumption that the intensity values are independent variables:

$$P(\mathbf{x}' \in \bar{\mathcal{O}}|I) = P(\mathbf{x}' \in \bar{\mathcal{O}}|u'),$$

where $u' = I(\mathbf{x}')$. Then Bayes rule leads to:

$$P(\mathbf{x}' \in \bar{\mathcal{O}}|I) = \frac{P(\mathbf{x}' \in \bar{\mathcal{O}}).P(u'|\mathbf{x}' \in \bar{\mathcal{O}})}{P(u')}$$

and thus equation (12) becomes :

$$p_T(\mathbf{x}|I,\lambda) = \begin{cases} \frac{(1-\alpha_i)p_e(I(\mathbf{x}'))}{\alpha_i p_i(I(\mathbf{x}'))+(1-\alpha_i)p_e(I(\mathbf{x}'))} & \text{if } \lambda \in \Lambda_i \\ \\ \frac{\alpha_i p_i(I(\mathbf{x}'))}{\alpha_i p_i(I(\mathbf{x}'))+(1-\alpha_i)p_e(I(\mathbf{x}'))} & \text{if } \lambda \in \Lambda_e \end{cases} \tag{13}$$

The data consistency term h_I at point $\mathbf{x}$ belonging to the interface is defined as a decreasing function of $p_T(\mathbf{x}|I,\lambda)$. Since this probability is only defined on the interface, h_I is extended to $\mathbb{R}^3$ via a windowing function related to the closest point $\tilde{\mathbf{x}}$ to $\mathbf{x}$ on the interface:

$$h_I(\mathbf{x}) = g[p_T(\tilde{\mathbf{x}}|I,\lambda)] \qquad \forall \mathbf{x} \in \mathbb{R}^3, \tag{14}$$

where g is the decreasing function illustrated in Figure 5 and given by :

$$g(x) = \begin{cases} 1-4x^3 & = \text{if } x < 0.5 \\ 4(1-x)^3 & = \text{otherwise} \end{cases} \tag{15}$$

4.4 Step size Δt

The step size Δt of equation (3) is usually fixed as constant and manually tuned as a trade-off between speed of convergence and stability of the process, which is hardly compatible with practical applications. We propose to evaluate it automatically at each iteration in order to improve robustness.

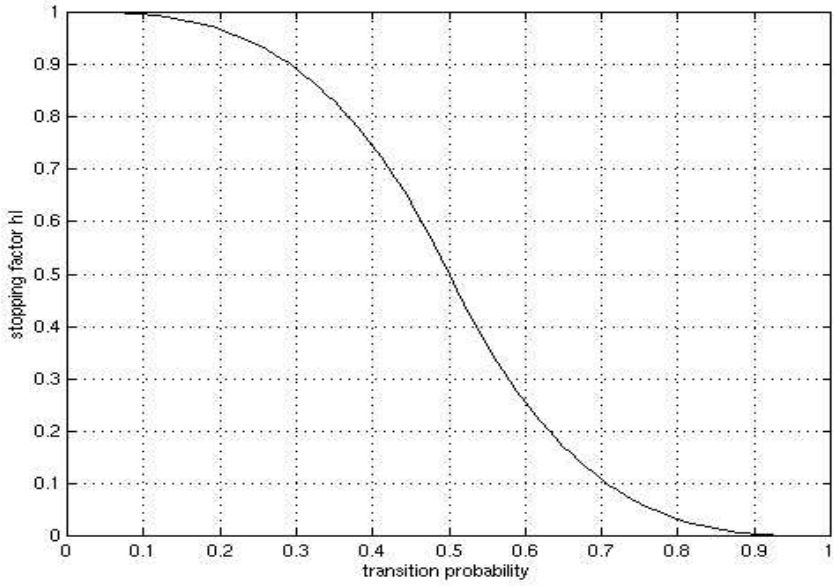

Figure 5: Stopping factor h_I as a decreasing function of the posterior transition probability $p_T(\mathbf{x}|I,\lambda)$ of point $\mathbf{X}$ to be a transition in the image.

The stability of the process requires a numerical scheme for the computation of $\nabla\Psi$, called *upwind scheme* [20]. This scheme induces a limit on the step size Δt, called the CFL restriction (Courant-Friedrichs-Levy). More precisely, writing equation (2) as $\Psi_t + H(\Psi_x, \Psi_y, \Psi_z) = 0$, where H is the Hamiltonian defined by:

$$H(u, v, w) = \sqrt{u^2 + v^2 + w^2}.F, \tag{16}$$

the CFL restriction can be expressed in 3D [16] as:

$$\Delta t.(\frac{|H_u|}{\Delta x} + \frac{|H_v|}{\Delta y} + \frac{|H_w|}{\Delta z}) \leq 1,$$

where H_u, H_v, H_w denote the partial derivatives of H with respect to u, v, w. Since we work with a regular sampling grid, we can assume $\Delta x = \Delta y = \Delta z = 1$. As a result, the maximal value for Δt which guarantees the stability of the numerical scheme is given by:

$$\widehat{\Delta t} = \min\{\frac{1}{|H_u| + |H_v| + |H_w|}\}$$

We propose to evaluate this value at each iteration of the process. According to equation (4) and the definition of its parameters, the speed function F is independent from u, v, w. The terms h_I and ν only depends on the image data. The curvature term κ is the curvature of the interface at the closest point, and it does not depend on the local characteristics of Ψ. Therefore the partial derivatives of H can be directly computed from (16), and the best value for Δt which guarantees stability is given by:

$$\widehat{\Delta t} = \min\{\frac{1}{F}.\frac{\sqrt{u^2 + v^2 + w^2}}{|u| + |v| + |w|}\} \tag{17}$$

4.5 Stopping criterion

The iterative propagation process stops when the two following conditions are met:

1. the ratio of new voxels to the total number of voxels in the volume (per iteration) is below a threshold $\epsilon_1 = 0.001$,
2. the first derivative of the displacement function, defined as the average value of h_I over the interface, is below a threshold $\epsilon_2 = 0.01$.

The choice of these values expresses a trade-off between the accuracy of the detection and the speed of convergence. They have been empirically determined from our experiments. However, the quality of the results does not appear to be very sensitive to these choices (see Figure 7 for an example of surface evolution).

5 Experimental Results

5.1 Synthetic data and numerical assessment

The segmentation algorithm was run on simulated brain MR images provided by the MNI [8] and available on the web [1]. The input to the simulator is a 3D brain model with labelled grey matter, white matter, and cerebrospinal fluid, which is manually generated from a volumetric MRI data set. Given this labelled volume, signal intensities are computed using the signal production simulation, then mapped to produce a pseudo-MRI volume. The image can be simulated under ideal noiseless conditions or with a noise level dependent on imaging parameters. This includes effects such as noise and spatial inhomogeneities of the magnetic field.

The head phantom was collected with 3 levels of noise and inhomogeneity (size $181 \times 217 \times 181$). The method was applied to segment the whole brain (grey matter + white matter) in the head phantom. It was numerically assessed with the following overlapping measures [32]:

$$\begin{cases} \text{sensitivity} & = TP/(TP+FN) \\ \text{specificity} & = TN/(FP+TN) \\ \text{total performance} & = (TP+TN)/(TP+FP+TN+FN), \end{cases} \tag{18}$$

where TP, TN, FP and FN respectively denote the number of true positive, true negative, false positive and false negative points, computed according to the reference classification associated to the phantom. A low sensitivity value indicates under-segmentation, whereas a low specificity value indicates over-segmentation.

The segmentation was initialized with a cube $100 \times 70 \times 70$, and the classes of interest (grey matter + white matter) automatically determined as described in section 3. The results of the segmentation are shown in Figure 6. It was compared with a segmentation method based on morphological operators [13, 34] and tuned with a "best practice" parameter set. The numerical assessment of both methods is summarized in Table 1. The total performance achieved with our algorithm is stable around 98.3%, even in critical conditions (9% noise and 40% inhomogeneity). This outperforms the other method whose behaviour is very dependent on noise. The improvement mainly concerns the sensitivity of the detection.

Figure 7 plots the evolution of the average speed and the evolution of the volume size, with respect to the number of iterations. The speed decreases until an almost constant value (strictly positive), whereas the size of the volume regularly increases. This justifies the choice of our stopping criterion mentioned in subsection 4.5.

5.2 Segmentation of real MR images

Experiments have also been run on a database of 18 different MR volumes (volume size $256 \times 256 \times 176$). All the volumes have been processed in the same way, and using *exactly the same parameter set*. The step size and the probability density functions are automatically computed. The weighting parameters on regularization have been set to $\rho^+ = 3$ and $\rho^- = 1$ (see subsection

[1] http://www.bic.mni.mcgill.ca/brainweb

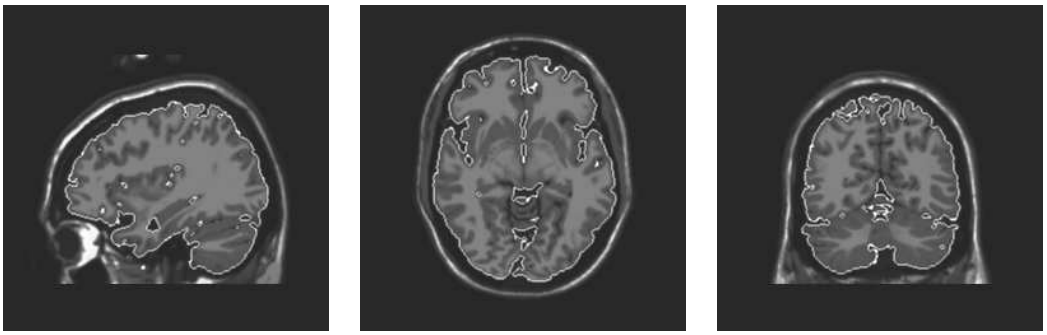

Figure 6: Segmentation of the brain phantom. The three columns respectively show saggital, axial and coronal planes. The volume consists of $181 \times 217 \times 181$ voxels and was simulated under ideal noiseless conditions.

	Levels sets				Morphological approach		
	Nb iter	Sens.	Spec.	Total	Sens.	Spec.	Total
0% noise, 0% inhom.	710	96.2%	99.0%	98.3%	86.7%	98.7%	95.7%
3% noise, 20% inhom.	680	96.3%	98.9%	98.2%	83.5%	99%	95.2%
9% noise, 40% inhom.	800	95.95%	98.9%	98.2%	69.8%	99.5%	92.3%

Table 1: Quantitative assessment on the phantom. The number of iterations, the sensitivity, specificity, and total performance measures are given for three levels of noise and two segmentation methods: our method based on level sets (initialization with a cube $100 \times 70 \times 70$) and a segmentation method based on morphological operators.

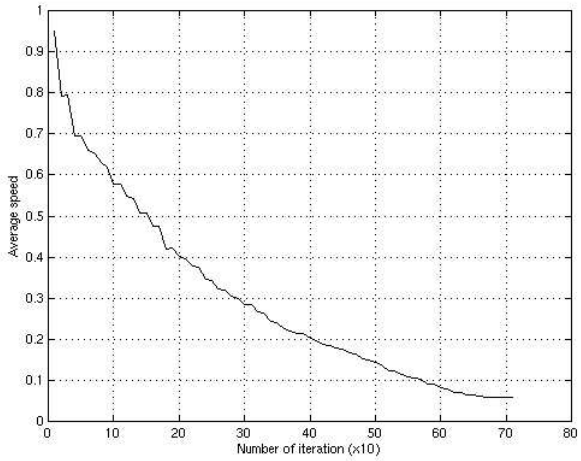

(a)

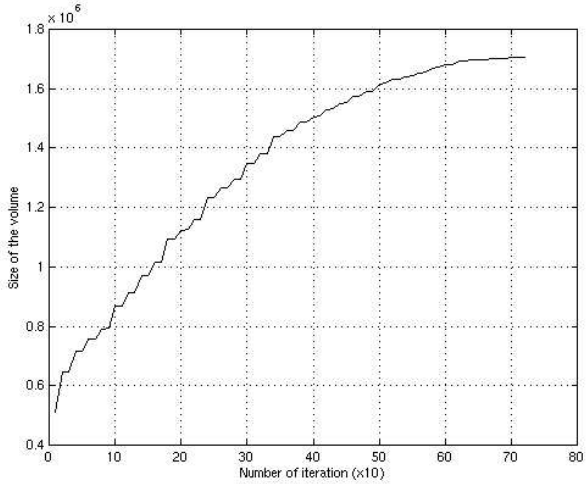

(b)

Figure 7: Evolution of the displacement function (a) and of the size of the volume (b) with respect to the number of iterations, for the phantom brain shown in Figure 6. The displacement function is defined as the average value of the stopping factor h_I over all the points of the interface.

4.2), which has appeared to be a good compromise to avoid propagation out of the brain (possible when the cerebro-spinal fluid area is thiner than the image resolution), whilst preserving the highly convoluted characteristics of the cortical surface. Out of the 18 subjects, only one segmentation failed because the cerebro-spinal fluid area was locally too thin, and there was no clear separation between grey matter, fat and dura matter. However the failure could be automatically detected because the propagation speed started to increas, whereas it should keep decreasing. All the other 17 subjects were correctly segmented. This corresponds to a success ratio of 94%, which be considered as satisfactory in a clinical use context. Figures 8 and 9a report the segmentation results on three subjects. Protusions of brain and ventricles are properly recovered. The method can naturally cope with change of topology. On average, 1000 iterations are necessary to segment the whole brain on real data starting from a $100 \times 70 \times 70$ cube. The number of iterations can be reduced to 300 if the surface is initialized close to the real boundaries by a registration technique as we have proposed in [2, 3].

The same method can be applied to the segmentation of a particular class of tissue (white matter, grey matter, cerebro-spinal fluid). For this purpose, one just has to provide a coarse intensity value characterizing the class as an input parameter, or to initialize the surface with a small cube located inside the tissu. The process is exactly the same as for segmenting the whole brain. This can be used for separating white matter from grey matter for instance. Figure 9b shows the white matter detected using this technique. The surface was initialized with the segmentation shown in Figure 9a, and 310 iterations were necessary.

The method has also been successfully applied for segmenting ventricles. An example is shown in Figure 10.

5.3 Segmentation of 3D ultrasound images

The method has finally been applied to 3D ultrasound images of carotid artery. These volumes were acquired with a free-hand acquisition mode, based on the tracking and compounding of 2D echographic slices obtained with regular clinical devices [10, 26]. This kind of images is difficult to segment automatically because of speckle noise. In particular, image gradient information is most of the time irrelevant, and therefore a classical propagation model based on image gradient does not supply satisfying results.

Several studies have shown that the signal of accoustic imagery could be modeled by two kinds of distributions [22, 27, 31]. The reverberation areas are associated to speckle noise and can be modelled by a shifted Rayleigh distribution (see equation 5), whilst shadow areas are only related to electronic noise and can be modeled by a normal distribution. For this study, we have also used a bimodal model to represent ultrasound images. The intensity distribution outside the carotid is modelled by a shifted Rayleigh distribution because it stems from the reverberation of anatomical tissues. The area inside the carotid is a blood area with almost no accoustic reverberation, and it is therefore modelled by a normal distribution.

An example of intensity distribution of an ultrasound image is plotted in Figure 3, along with the corresponding estimated mixture. The estimated distribution mixture does not exactly fit the original

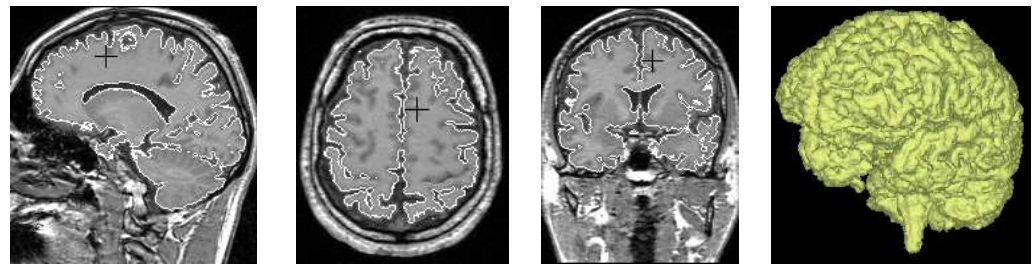

Subject 1

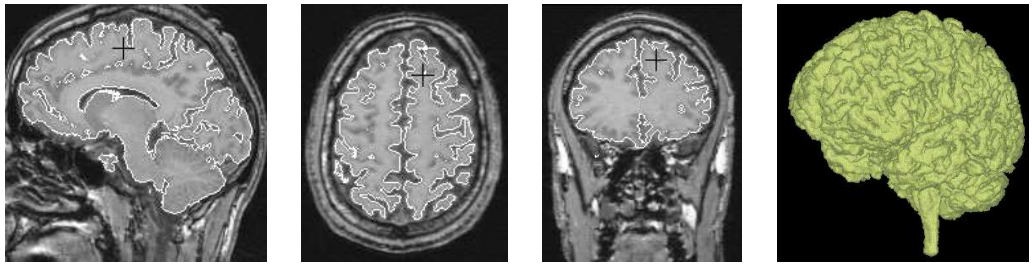

Subject 2

Figure 8: Brain segmentation for two different subjects. The first three columns respectively show saggital, axial and coronal planes, the last column shows 3-D views of the segmented brains. The volumes consist of $256 \times 256 \times 176$ voxels and were acquired in real conditions.

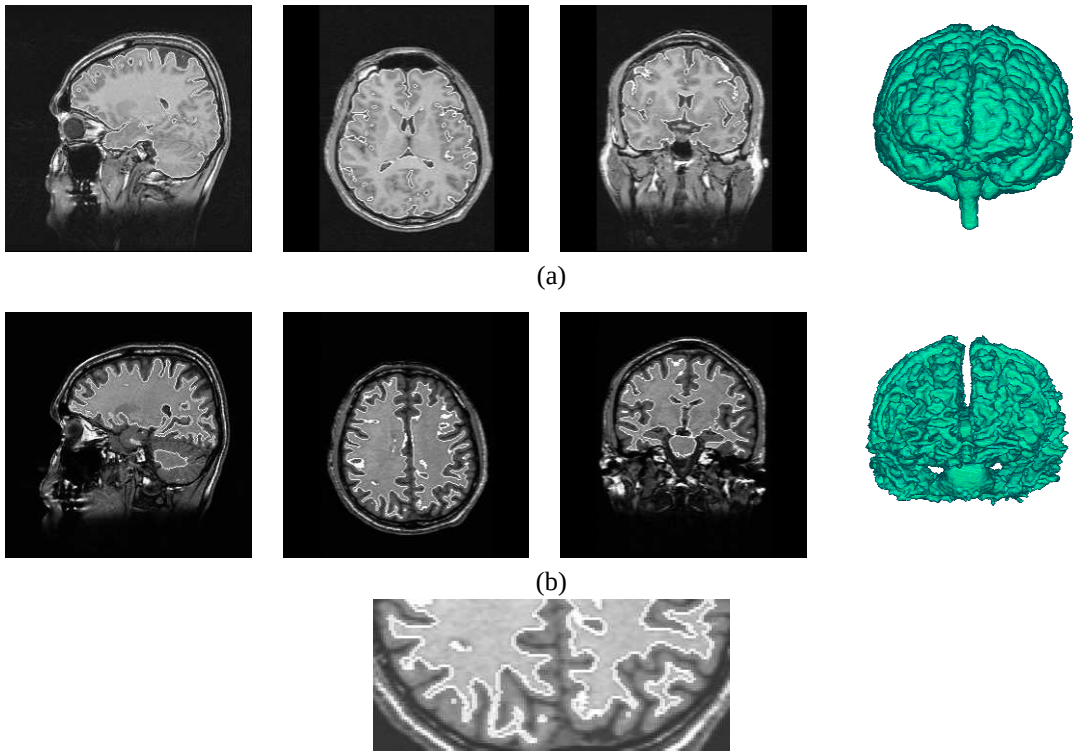

Figure 9: Segmentation of both grey and white matter on MR images : (a) Segmentation of the whole brain (grey matter + white matter) for subject 3. The first three columns respectively show saggital, axial and coronal planes, the last column shows a 3-D view of the segmented brain. (b) Segmentation of the white matter only; The surface was initialized with the result shown in (a), and 310 iterations were necessary. (c) Zoom on the detected white matter.

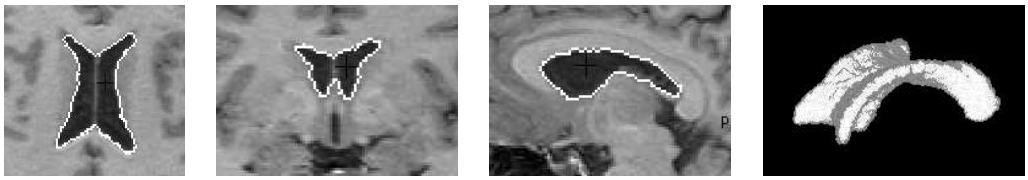

Figure 10: Ventricle segmentation. The process is the same as for the brain segmentation, only initialization differs (small cube coarsely located inside the ventricles). The first three columns respectively show axial, coronal and saggital planes, the last column shows a 3D view of the ventricles.

distribution because the bimodal approximation is too simple to accurately model the signal. This is due to the fact that anatomical tissues are not homogeneous and they should probably be modeled by several Rayleigh distributions. However, given the complexity of this issue on itself, we have limited our study to a bimodal approximation, which has been appropriate enough to separate the two main classes of the image. We have used a high weighting value for regularization ($\rho = 10$), in order to cope with the high level of noise. All the other parameters have kept the same values as for previous brain MRI experiments, which demonstrates a very stable behaviour over various experimental conditions. Figures 11 and 12 display the results of segmentation on two different ultrasound images. The carotid has been retrieved despite of the noise. Thanks to the evolution model based on region-based information, the surface converges to the right location even though there is locally no signal (very small image gradient). The algorithm is therefore more robust, and it is for instance able to separate two neighbouring blood or air cavities.

6 Conclusion and Further Work

This paper has presented a robust and adaptive deformable model for segmenting structures in 3D images using the Level Set formalism. The Level Set approach is very appropriate to segment anatomical structures without strong prior information. The statistical analysis of intensity distributions provides relevant information about input data. The design of an adaptive evolution force and an adaptive step size provides a good trade-off between convergence speed and stability. Almost no parameter needs to be tuned in our method, only the regularization weight ρ has to be set depending on the data shape and noise. Good quality results have been produced on brain MRI and 3D echographies of carotid. The results demonstrate that a variational approach mixed with region-based analysis based statistical models significantly improves the sensitivity and the robustness of the segmentation. Furthermore, thanks to the genericity of the method, the segmentation can be achieved for various image modalities and various kinds of anatomical structure.

The qualities of the method are especially interesting for processing 3D ultrasound imagery. Due to speckle noise, a method mixing variational and statistical models are particularly appropriate to achieve an accurate and efficient a segmentation. A further study would include the validation of the Rayleigh distribution for modeling the scattered signal in 3D echography. A mixture of

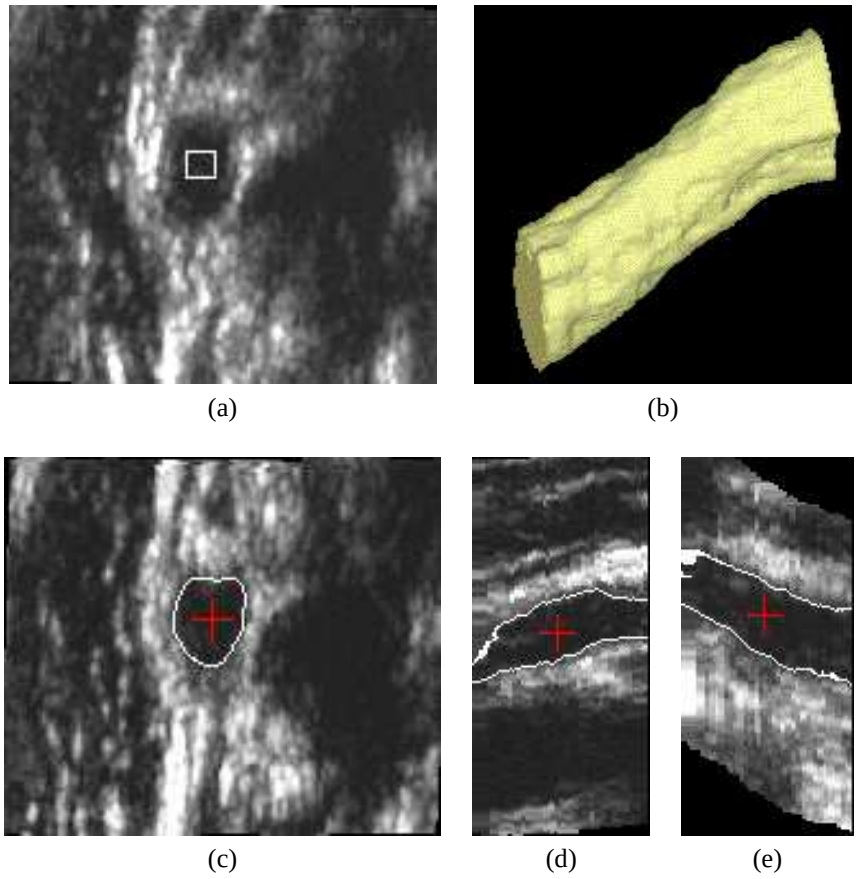

Figure 11: Segmentation result on a $256 \times 256 \times 80$ ultrasound image of carotid (isotropic voxels). (a) initialization of the segmentation with a $10 \times 10 \times 25$ cube. (b) 3D view of the segmented carotid. (c,d,e) three visualization planes of the final segmentation.

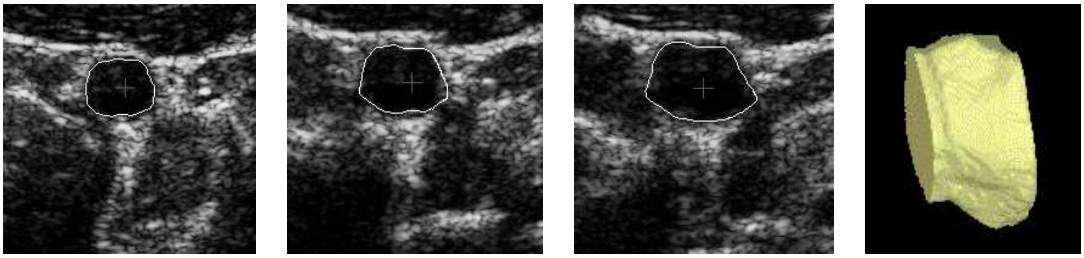

(a) (b) (c) (d)

Figure 12: Three transaxial slices (a,b,c) and a 3D view (d) of a segmented subpart of carotid (non isotropic voxels). The $256 \times 256 \times 36$ input image was initialized with a $50 \times 50 \times 25$ cube inside the carotid.

Rayleigh distributions could also be studied. Finally, it might be important to include statistical prior information about the shape of the anatomic structure in the propagation model.

Acknowledgements. The authors are very grateful to P. Hellier, from IRISA, for his assistance and helpful discussions. They would like to thank Drs L. Pourcelot and F. Tranquart from Tours university hospital and Dr A. Fenster from RRI (London, Ontario) for providing the US data, as well as the GIS "Sciences de la cognition" and the Brittany Region council for supporting the MR acquisition project.

References

[1] O. Amadieu, E. Debreuve, M. Barlaud, and G. Aubert. Inward and outward curve evolution using level set method. In *Proc of IEEE Int. Conf. on Image Processing*, Kobe, Japan, October 1999.

[2] C. Baillard, P. Hellier, and C. Barillot. Cooperation between level set techniques and dense 3d registration for the segmentation of brain structures. In *Int. Conference on Pattern Recognition*, volume I, pages 991–994, September 2000.

[3] C. Baillard, P. Hellier, and C. Barillot. Segmentation of brain 3D MR images using level sets and dense registration. *Medical Image Analysis Journal*, 2000. Submitted.

[4] V. Caselles, R. Kimmel, and G. Sapiro. Geodesic active contours. *Int. Journal of Computer Vision*, 22:61–79, 1997.

[5] G. Celeux and J. Diebolt. L'algorithme SEM : un algorithme d'apprentissage probabiliste pour la reconnaissance de mélanges de densités. *Revue de statistiques appliquées,* 34(2):35–51, 1986.

[6] A. Chakraborty, L. Staib, and J. Duncan. Deformable boundary finding in medical images by integrating gradient and region information. *IEEE Trans. on Medical Imaging*, 15(6):859–870, December 1996.

[7] L.D. Cohen. On active contour models and balloons. *Computer Vision, Graphics, and Image Processing*, 53(2):211–218, 1991.

[8] D.L. Collins, A.P. Zijdenbos, V. Kollokian, J.G. Sled, N.J. Kabani, C.J. Holmes, and A.C. Evans. Design and construction of a realistic digital brain phantom. *IEEE Transactions on Medical Imaging*, 17(3):463–468, June 1998.

[9] A.P. Dempster, N.M. Laird, and D.B. Rubin. Maximum likelihood from incomplete data via the EM algorithm. *Journal of Royal Statistical Society*, 3:1–38, 1976.

[10] A. Fenster and D.B. Downey. 3D ultrasound imaging: a review. *IEEE Engineering in Medicine and Biology*, 15(6):41–51, 1996.

[11] J. Gomes and O. Faugeras. Reconciling distance functions and Level-Sets. Technical Report 3666, Inria, April 1999.

[12] G. Hermosillo, O. Faugeras, and J. Gomes. Cortex unfolding using Level-Set methods. Technical Report 3663, Inria, April 1999.

[13] K. H. Hohne and W. A. Hanson. Interactive 3d segmentation of mri and ct volumes using morphological operations. *J. of Computer Assisted Tomography*, 16(2):285–294, 1992.

[14] M. Kass, A. Witkin, and D. Terzopoulos. Snakes: Active contour models. *Int. Journal of Computer Vision*, 1:321–331, 1988.

[15] C. Kervrann and F. Heitz. A hierarchical Markov modeling approach for the segmentation and tracking of deformable shapes. *Graphical Models and Image Processing*, 60(3):173–195, May 1998.

[16] R. Kimmel, N. Kiryati, and A. Bruckstein. Analyzing and synthesizing images by evolving curves with the Osher-Sethian method. *Int. Journal of Computer Vision*, 24(1):37–55, 1997.

[17] G. Le Goualher, C. Barillot, and Y. Bizais. Modeling cortical sulci with active ribbons. *Int. Journal of Pattern Recognition and Artificial Intelligence*, 8(11):1295–1315, 1997.

[18] L. M. Lorigo, O. Faugeras, W. E. L. Grimson, R. Keriven, and R. Kikinis. Segmentation of bone in clinical knee MRI using texture-based geodesic active contours. In A. Colchester and S. Delp, editors, *Medical Image Computing and Computer-Assisted Intervention*, volume 1496 of *LNCS*, pages 1195–1204, Cambridge, MA, USA, October 1998. Springer.

[19] R. Malladi, J.A. Sethian, and B.C. Vemuri. Shape modeling with front propagation: A level set approach. *IEEE Trans. on Pattern Analysis and Machine Intelligence*, 17(2):158–175, February 1995.

[20] R. Malladi, J.A. Sethian, and B.C. Vemuri. A fast level set based algorithm for topology-independent shape modeling. *J of Mathematical Imaging and Vision*, 6:269–289, 1996.

[21] P. Masson and W. Pieczynski. SEM algorithm and unsupervised statistical segmentation of satellite images. *IEEE Trans. on Geoscience and Remote Sensing*, 31(3):618–633, may 1993.

[22] M. Mignotte and J. Meunier. Deformable template and distribution mixture-based data modeling for the endocardial contour tracking in an echographic sequence. In *Proc of IEEE Int. Conf. on Computer Vision and Pattern Recognition*, pages 225–230, June 1999.

[23] S. Osher and J.A. Sethian. Fronts propagating with curvature dependent speed: Algorithms based on Hamilton-Jacobi formulation. *Journal of Computational Physics*, 79:12–49, 1988.

[24] C. Papin, P. Bouthemy, E. Mémin, and G. Rochard. Tracking and characterization of highly deformable cloud structure. In *European Conf. on Computer Vision*, volume LNCS 1843-2, pages 428–442, Dublin, Ireland, June 2000.

[25] N. Paragios and R. Deriche. Video and image sequence analysis - geodesic active contours and level sets for the detection and tracking of moving objects. *IEEE Trans. on Pattern Analysis and Machine Intelligence*, 22(3):266–280, 2000.

[26] R.W. Prager, A. Gee, and L. Berman. Stradx: real-time acquisition and visualization of free-hand three-dimensional ultrasound. *Medical Image Analysis Journal*, 3(2):129–140, 1998.

[27] F. Schmitt, M. Mignotte, C. Collet, and P. Thourel. Estimation of noise parameters on sonar images. In *Signal and Image processing*, number 2823 in SPIE, pages 1–12, Denver, Colorado, aug 1996.

[28] P. Schroeter, J.-M. Vesin, T. Langenberger, and R. Meuli. Robust parameter estimation of intensity distributions for brain magnetic resonance images. *IEEE Trans. on Pattern Analysis and Machine Intelligence*, 17(2):172–186, April 1998.

[29] L.H. Staib and J.S Duncan. Model-based deformable surface finding for medical images. *IEEE Trans. on Medical Imaging*, 16:720–731, 1996.

[30] D. Terzopoulos. Regularization of inverse visual problems involving discontinuities. *IEEE Trans. on Pattern Analysis and Machine Intelligence*, 8(2):413–424, 1986.

[31] P. Thourel. *Segmentation d'images sonar par modélisation markovienne hiérarchique et analyse multi-résolution*. PhD thesis, Université de Bretagne Occidentale, July 1996.

[32] JH. Van Bemmel and MA. Musen. *Handbook of medical informatics*. Springer, URL : http://www.mieur.nl/mihandbook, 1997.

[33] A. Yezzi, A. Tsai, and A. Willsky. Binary and ternary flows for image segmentation. In *Proc of IEEE Int. Conf. on Image Processing*, Kobe, Japan, October 1999.

[34] J. Ylä-Jääski, F. Klein, and O. Kübler. Fast direct display of volume data for medical diagnosis. *Computer Vision, Graphics, and Image Processing*, 53(1):7–18, 1991.

[35] X. Zeng, L.H. Staib, R.T. Schultz, and J.S. Duncan. Segmentation and measurement of the cortex from 3D MR images using coupled surfaces propagation. *IEEE Trans. on Medical Imaging*, 18(10):148–157, October 1999.

[36] X. Zeng, L.H. Staib, R.T. Schultz, H. Tagare, L. Win, and J.S. Duncan. A new approach to 3D sulcal ribbon finding from MR images. In C. Taylor and A. Colchester, editors, *Medical Image Computing and Computer-Assisted Intervention*, volume 1679 of *Lecture Notes in Computer Science*, pages 148–157. Springer, September 1999.

[37] S.C. Zhu and A. Yuille. Region competition: Unifying snakes, region growing, and Bayes/MDL for multiband image segmentation. *IEEE Trans. on Pattern Analysis and Machine Intelligence*, 18:884–900, 1996.

Unité de recherche INRIA Lorraine, Technopôle de Nancy-Brabois, Campus scientifique,
615 rue du Jardin Botanique, BP 101, 54600 VILLERS LÈS NANCY
Unité de recherche INRIA Rennes, Irisa, Campus universitaire de Beaulieu, 35042 RENNES Cedex
Unité de recherche INRIA Rhône-Alpes, 655, avenue de l'Europe, 38330 MONTBONNOT ST MARTIN
Unité de recherche INRIA Rocquencourt, Domaine de Voluceau, Rocquencourt, BP 105, 78153 LE CHESNAY Cedex
Unité de recherche INRIA Sophia-Antipolis, 2004 route des Lucioles, BP 93, 06902 SOPHIA-ANTIPOLIS Cedex

Éditeur
INRIA, Domaine de Voluceau, Rocquencourt, BP 105, 78153 LE CHESNAY Cedex (France)
http://www.inria.fr
ISSN 0249-6399